INORGANIC CHEMISTRY FRONTIERS

RESEARCH ARTICLE

View Article Online
View Journal | View Issue



Cite this: *Inorg. Chem. Front.*, 2025, **12**, 3637

# VRBE and HRBE schemes of lanthanides: design of dual-luminescence-center long persistent luminescence phosphors with $Pr^{3+}$ or/and $Tb^{3+}$ doping in $Mg_3Y_2Ge_3O_{12}$ garnet with high storage capacity for anti-counterfeiting, information storage, and X-ray imaging†

Yuanying Lin,[a] Chengzhuo Ming,[a] Ruonan Xuan[b] and Weisheng Liu *[a]

Received 7th November 2024,
Accepted 19th February 2025

DOI: 10.1039/d4qi02823f

rsc.li/frontiers-inorganic



The development of X-ray charged long persistent luminescence (LPL) phosphors with excellent storage capacity remains a significant challenge. These phosphors have multifunctional applications in white light-emitting diodes (w-LEDs), multi-mode anti-counterfeiting, information storage, and X-ray imaging. Herein, by combining the refined chemical shift model, optical spectroscopy, and thermoluminescence (TL) curves, the host-referred and vacuum-referred binding energy (HRBE and VRBE) schemes about $Mg_3Y_2Ge_3O_{12}:Ln^{3+}$(MYGO:Ln, Ln = Pr or/and Tb) phosphors are constructed and validated. MYGO:Pr,Tb avoids the re-absorption issue in the blue light region and agrees well with blue phosphors for w-LED applications. MYGO:Pr,Tb Charged with X-rays (Xc), the TL intensity ratios to commercial $SrAl_2O_4:Eu^{2+}$, $Dy^{3+}$/BaFBr(I):$Eu^{2+}$ are 1.517 and 1.435, respectively, and 50% of the carriers remain for over 1000 h. Finally, the MYGO series phosphors are successfully applied in multi-mode anti-counterfeiting, information storage, and X-ray imaging.

## 1. Introduction

Since the discovery of X-rays, they have played a central role in various aspects of human life. In particular, X-ray indirect detection has found widespread applications in medical imaging, industrial machinery nondestructive testing, civil aviation security inspections, and nuclear physics engineering.[1–11] The key to X-ray indirect detection lies in the ability of imaging materials to absorb X-rays and convert them into visible luminescence signals.[11–14] Halide chalcogenide scintillators, as conventional X-ray imaging materials, offer high light yield but are often complex to synthesize, produce significant pollutants, and suffer from poor stability due to decomposition caused by water, air, or ionizing radiation.[15–21] These limitations have hindered their broader commercial applications. Long persistent luminescence (LPL) storage materials have emerged as a promising alternative, offering advantages such as ease of synthesis, environmental friendliness, and high stability. These materials overcome the drawbacks of traditional halide chalcogenide scintillators and are being increasingly used to meet societal demands for efficient information storage.[22–29] Additionally, LPL materials play an important role in multi-mode anti-counterfeiting, battery-free radiation dose measurement, X-ray imaging, and high-capacity storage.[23,25,26,30–34]

Luminescence centers are a key component of phosphors, determining their emission range.[23,25,26] To date, green LPL phosphors such as $SrAl_2O_4:Eu^{2+},Dy^{3+}$ and BaFBr(I):$Eu^{2+}$, where a single lanthanide ion serves as the luminescence center, remain the benchmark for LPL and storage materials. However, red and yellow phosphors are relatively scarce.[25,26,35] Moreover, conventional yellow phosphors suffer from re-absorption in the blue light region and lack red spectral components, resulting in low color rendering and uneven white light tones in novel lighting applications such as w-LEDs.[36] Dual-luminescence-center yellow LPL materials can overcome these issues, enabling proportional chemical sensing, multi-color displays, and imaging, thereby advancing complex anti-counterfeiting technologies. These characteristics make the

[a]*College of Chemistry and Chemical Engineering, Lanzhou University, Lanzhou 730000, PR China. E-mail: liuws@lzu.edu.cn; Tel: +86-18993168326*
[b]*School of Chemistry and Chemical Engineering, Qinghai Normal University, Xining 810008, PR China*

† Electronic supplementary information (ESI) available. See DOI: https://doi.org/10.1039/d4qi02823f

development of dual-luminescence-center LPL materials a reasonable strategy for encryption of military information and multi-mode anti-counterfeiting applications.

Traps are another crucial component of phosphors, as their concentration and depth significantly influence LPL and storage properties.[21,23,37] While the LPL mechanism remains insufficiently understood, accurate methods for predicting trap depths are in high demand.[23] The host-referred and vacuum-referred binding energy (HRBE and VRBE) schemes, based on Dorenbos' theory, enable the determination of energy levels for divalent and trivalent lanthanide ions and the prediction of trap depths.[38–40] Efficient LPL and storage phosphor design can be achieved by adjusting the type and concentration of lanthanide ions to regulate the trap depth and carrier distribution.[23] However, HRBE and VRBE schemes have thus far been applied to only a limited number of materials.[25]

This study focuses on the development of dual-luminescence-center yellow LPL materials for X-ray imaging and anti-counterfeiting applications. In 2020, Jiang *et al.* first reported a $Mg_3Y_2Ge_3O_{12}$:$Ce^{3+}$ (MYGO:Ce) garnet phosphor and achieved red-shifted $Ce^{3+}$ emission by substituting $Ge^{4+}$ with $Si^{4+}$ to enlarge the host bandgap.[41] Subsequent studies by Liao *et al.*, Hou *et al.*, and Meng *et al.* introduced various dopants such as $Eu^{3+}$, $Ce^{3+}$, and $Bi^{3+}$, enhancing properties like thermal stability, tunable luminescence, and extended LPL durations.[42–44] Recently, Krieke *et al.* reported MYGO:$Tb^{3+}$, a garnet LPL phosphor with bright blue-green tunable luminescence.[45] These findings suggest that the MYGO host has the potential for achieving dual-luminescence-center LPL materials with multifunctional applications. In this work, we successfully constructed the HRBE and VRBE schemes for MYGO, predicting trap depths of 1.68 eV and 1.86 eV for $Pr^{3+}$ and $Tb^{3+}$, respectively. These depths meet the requirements for high-capacity information storage, which typically requires trap depths greater than 1.00 eV. This study provides valuable insights for advancing the development of multi-mode optical anti-counterfeiting materials and information encryption technologies. Regarding the LPL performance of MYGO:Ln (MYGO:Pr, MYGO:Tb, and MYGO:Pr,Tb), the $\tau_p$, $\tau_t$, and $\tau_c$ values under 254 nm ultraviolet (UV) lamp charging ($U_c$) were approximately 405, 179, and 48 min, respectively. Additionally, the initial LPL intensities for all three types exceeded 100 mcd $m^{-2}$. MYGO:Pr ($\tau_p$ = 405 min) demonstrated a significant advantage among lanthanide-activated red LPL materials. As a dual-luminescence-center system, $Pr^{3+}$ and $Tb^{3+}$ produced distinct emission responses, enabling MYGO:Pr,Tb to exhibit yellow LPL under $U_c$. This exceptional performance highlights its potential for multi-level anti-counterfeiting applications. Regarding the storage performance of MYGO:Ln, the experimental trap depths of $Pr^{3+}$ and $Tb^{3+}$, derived from the thermoluminescence (TL) curves of MYGO:Pr,Tb under X-ray charging ($X_c$), were measured as 1.684 and 1.867 eV, respectively. These values align well with the predictions from the HRBE and VRBE schemes. Additionally, the $X_c$ TL curves indicated that 49% of the carriers stored in MYGO:Pr,Tb remained intact after 1000 h. When compared to commercial phosphors $SrAl_2O_4$:$Eu^{2+}$,$Dy^{3+}$/BaFBr(I):$Eu^{2+}$, the TL intensity ratios ($r_1/r_4$, $r_2/r_5$, and $r_3/r_6$) for MYGO:Pr, MYGO:Tb, and MYGO:Pr,Tb were higher, with values of 1.298/1.228, 0.504/0.477, and 1.517/1.435, respectively. These results further emphasize the superior storage performance of MYGO:Ln phosphors. The LPL mechanism model elucidated the storage and release processes of carriers, identified defect types and trap depths, and detailed the energy level transitions and emission processes of the dual-luminescence centers, $Pr^{3+}$ and $Tb^{3+}$. Through comprehensive analyses of photoluminescence (PL), LPL, TL, and thermally stimulated luminescence (TSL) properties of MYGO:Pr, MYGO:Tb, and MYGO:Pr,Tb (MYGO:Ln), the multifunctional applications of deep-trap LPL phosphors in multi-mode anti-counterfeiting, information storage, and X-ray imaging have been realized. This study provides a robust theoretical foundation and experimental framework for further prediction and validation of energy levels in lanthanide-doped garnets. It also offers a theoretical perspective for the rational design of novel LPL and storage phosphors.

## 2. Results and discussion

### XRD and DRS of MYGO

$Mg_3Y_2Ge_3O_{12}$ (MYGO) is a unique garnet due to its multiple cationic lattice sites and structural properties that allow multiple cations to occupy the same lattice site. This characteristic facilitates the formation of a distorted lattice environment and complex traps.[45,46] For $A_3B_2C_3O_{12}$ garnets, there are three distinct cationic sites: the dodecahedral A site with a coordination number (CN) of 8, the octahedral B site (CN = 6), and the tetrahedral C site (CN = 4).[47] The ionic distribution in these sites is primarily determined by the relative size of the ions: larger cations occupy the A site, medium-sized cations are located in the B site, and smaller cations reside in the C site. However, MYGO belongs to a group called inverse garnets, analogous to inverse spinels.[46] The XRD patterns of MYGO:Ln are shown in Fig. 1(a) and Fig. S1.† The recorded patterns align well with the standard reference card for MYGO (no. AMCSD#0016886), confirming that all MYGO:Ln samples are single phase.[46,47]. As shown in Fig. 1(a), the slightly leftward shift of the XRD peaks ($2\theta$ values) with increasing concentrations of $Pr^{3+}$ and/or $Tb^{3+}$ is attributed to their larger ionic radii ($Pr^{3+}$: 1.126 Å, $Tb^{3+}$: 1.040 Å) compared to $Y^{3+}$ (1.019 Å) for CN = 8. This shift indicates lattice expansion in the garnet structure.[24–26,45] The structural model of MYGO is presented in Fig. 1(b). In the MYGO structure, $Mg^{2+}$ (0.89 Å) shares the dodecahedral A position with $Y^{3+}$ despite their significant differences in ionic radii. Consequently, the chemical formula can be expressed as $(Y_2Mg)Mg_2Ge_3O_{12}$.[45] This substitution distorts the local environment, promoting the formation of cationic and anionic vacancies, which enhance luminescence properties. Considering the similarity in ionic radii and coordination numbers, it is reasonable for lanthanide ions (Ln) to occupy the $Y^{3+}$ site (Y/$MgO_8$ dodecahedron) as luminescence centers.[45] To further investigate the crystal structure, XRD pat-

 

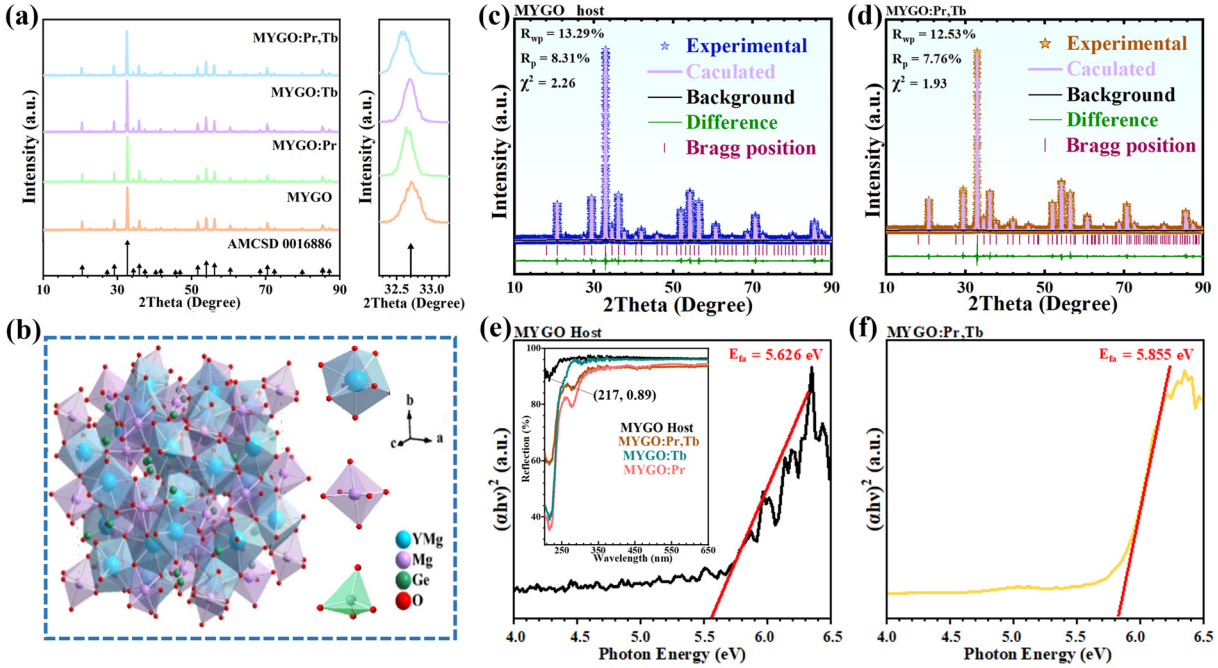


**Fig. 1** (a) X-ray diffraction patterns of the as-synthesized MYGO:Ln and detailed X-ray diffraction patterns from 32.25° to 33.25°. (b) Crystallographic structure of the MYGO host. [$Y/MgO_8$] dodecahedron, [$MgO_6$] octahedra and [$GeO_4$] tetrahedra are shown. (c and d) Rietveld refinement performed on the XRD data of the MYGO host (c) and MYGO:Pr,Tb (d). (e and f) DRS of the MYGO host (e) and MYGO:Pr,Tb (f).

terns were analyzed using Rietveld refinement, as shown in Fig. 1(c and d), Fig. S2a, b, and Table S2.† The refinement results show good convergence, with $\chi^2$ values of 2.26 (host), 2.08 (Pr), 2.17 (Tb), and 1.93 (Pr,Tb), respectively. These results confirm that the crystal system of MYGO:Ln is an inverse-garnet-type cubic structure, based on the *Ia3d* (230) space group.

To investigate the absorption properties of the host, the ultraviolet-visible diffuse reflectance spectra (UVV-DRS) at room temperature (RT) are presented in the inset of Fig. 1(e). According to the Mott and Davis theory, the fundamental absorption threshold ($E_{fa}$) values of the samples were calculated as 5.626 (host) 5.888 (Pr), 5.849 (Tb) and 5.855 (Pr and Tb) eV, as shown in Fig. 1(e, f) and Fig. S2c, d.†[23,48,49] Due to the relatively coarse DRS data for the host, the $E_{fa}$ value of 5.626 eV calculated by extrapolation from eqn (S1) and (2)† may not be entirely accurate. This is corroborated by the smoother DRS curves of MYGO:Ln, which provide more reliable results. The UVV-DRS and absorption curves (inset of Fig. S2c†) reveal that an absorption band with a peak at 217 nm (5.714 eV) is present in both MYGO:Ln and the host. This band is attributed to the fundamental absorption threshold of the host. Based on this common feature, the $E_{fa}$ value of the host was corrected to 5.714 eV, providing a more reasonable and accurate estimate. Notably, the absorption edge was found to be blue-shifted, and the detailed calculations and underlying reasons for this blue shift are explained in Fig. S2† in the discussion section. The SEM images of MYGO:Ln (Fig. S3a–d†) show that the samples consist of spherical particles with sizes ranging from approximately 0.3 μm to 5 μm. The EDS analysis (Fig. S3e–h†) confirms that $Ln^{3+}$ ions are effectively doped into the MYGO lattice.

## HRBE and VRBE schemes in MYGO

To analyze the trapping and releasing processes of charge carriers, the VRBE and HRBE schemes in MYGO have been constructed and exploited. A unique feature of the VRBE and HRBE schemes is their ability to compare the binding energy of electrons in the conduction band (CB), valence band (VB), or 4f ground states (GS) of lanthanides across various compounds using a common energy reference.[23–26] The $E_{fa}$ of MYGO is 5.714 eV. The band gap, influenced by electron–hole binding energy and temperature, is approximately calculated using Formula (1) as a rule of thumb:[39,50]

$$E_{ex} = E_{fa} + 0.008(E_{ex})^2 \quad (1)$$

where $E_{ex}$ is the band gap energy. Correcting $E_{ex}$ by including the electron–hole binding energy ($0.008E_{ex}$) gives a value of 6.00 eV. Fig. 2(a) and Fig. S2e† display the PLE and PL spectra, along with the PL process of MYGO:Ce. Two broad excitation bands ($\lambda_{em}$ = 537 nm) at 321 nm and 440 nm, along with an emission band ($\lambda_{ex}$ = 321 nm) at 537 nm, are observed in Fig. 2(a). The schematic energy level structure of a free gaseous $Ce^{3+}$ ion is shown in Fig. S2e,† illustrating the $Ce^{3+}$ ion at the $Y^{3+}$ site in MYGO:Ce.[51] The $Ce^{3+}$ emission arises from transitions between the lowest 5d excited state and the $^2F_{5/2}$ and $^2F_{7/2}$ GS. The PLE spectrum in Fig. 2(d) is decomposed *via*

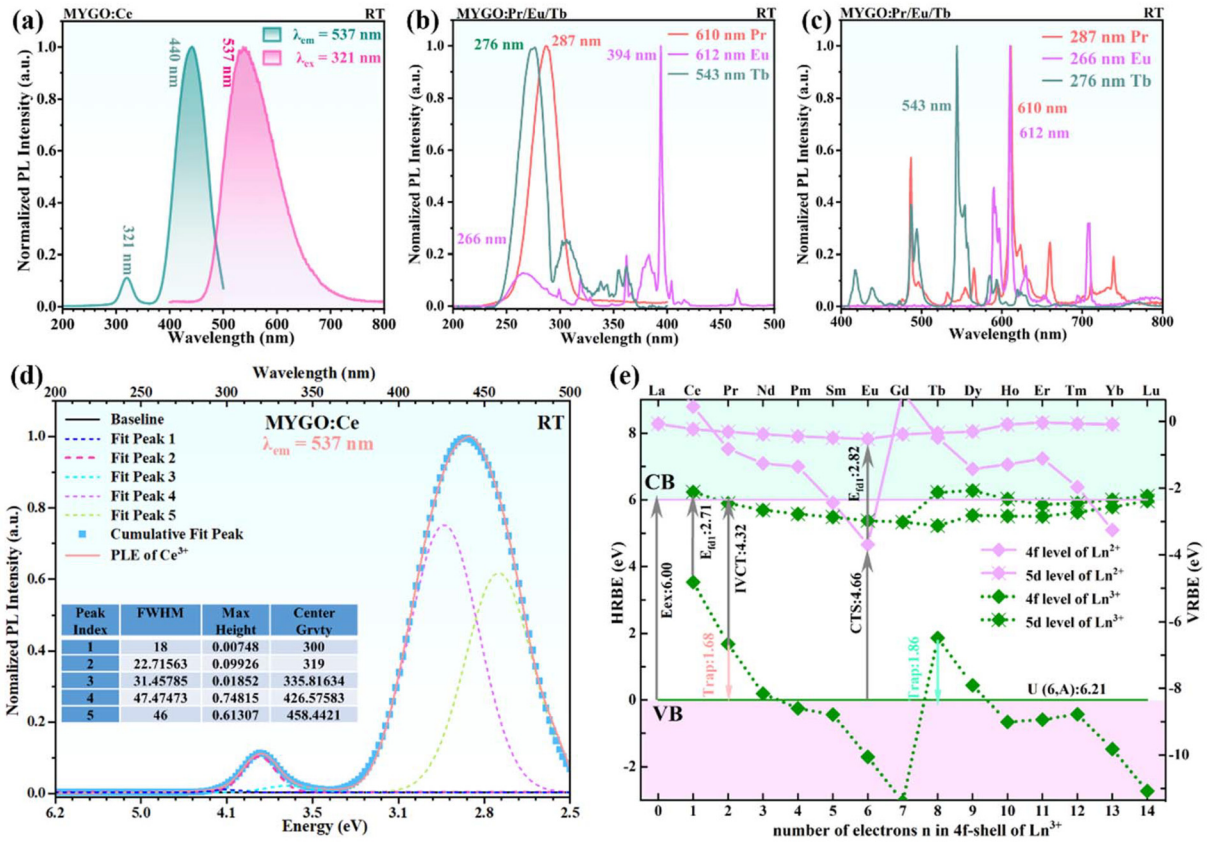


**Fig. 2** (a) The PLE ($\lambda_{em}$ = 537 nm) and PL ($\lambda_{ex}$ = 321 nm) spectra of the MYGO:Ce material. (b and c) The PLE (b) and PL (c) spectra of the phosphors MYGO:Pr/Eu/Tb. (d) The PLE ($\lambda_{em}$ = 537 nm) spectrum and the five fitted excitation bands at 300.0, 319.0, 335.8, 426.6 and 458.4 nm (4.13, 3.91, 3.70, 2.96, and 2.71 eV), respectively. (e) The HRBE and VRBE schemes in the MYGO system.

Gaussian fitting into five excitation bands at 300.0, 319.0, 335.8, 426.6, and 458.4 nm (4.13, 3.89, 3.69, 2.91, and 2.71 eV, respectively). The fit parameters for the PLE spectrum of MYGO:Ce confirm reliable results (Table S3†). The PLE and PL spectra of MYGO:Eu/Pr/Tb are shown in Fig. 2(b and c). The spectrum of MYGO:Eu clearly shows the $Eu^{3+}$ charge-transfer band (CTS) at 4.66 eV (266 nm). The electron transition from the 4f GS of $Pr^{3+}$ or $Tb^{3+}$ to the conduction band bottom is termed intervalence charge transfer (IVCT). For MYGO:Pr, the $Pr^{3+}$ IVCT band is located at 4.32 eV (286 nm). The empirical formulas (2) and (3) proposed by Dorenbos are as follows:[39,51–53]

$$U(6,A) = 5.44 + 2.834\exp(-\varepsilon_c/2.2) \quad (2)$$

$$E_{4f}(7,2+,A) = -24.92 + [18.05 - U(6,A)] \times [0.777 - 0.0353 \times U(6,A)]^{-1} \quad (3)$$

where $U$(6, A) represents the Coulomb repulsive force of $Eu^{3+}$/$Eu^{2+}$; $\varepsilon_c$ is the difference between the average excitation energy and that of free gaseous $Ce^{3+}$ (6.35 eV); $E_{4f}$ (7, 2+, $A$) is the energy of the $Eu^{2+}$ 4f GS in the VRBE column. Based on the PLE spectrum of MYGO:Ce and Dorenbos theory, the average energy of $Ce^{3+}$ 5d states and the $Ce^{3+}$ 4f–5d transition energy ($E_{fd1}$) are calculated as 3.47 eV and 2.71 eV, respectively. Thus, $\varepsilon_c$ is calculated to be 2.88 eV. Finally, $U$(6, A) and $E_{4f}$ (7, 2+, $A$), calculated using formulas (2) and (3), are 6.21 eV and −3.71 eV, respectively. The original data based on Dorenbos theory are provided in Table S4.† Collectively, the HRBE and VRBE schemes shown in Fig. 3(e) provide critical insights into the energy levels of lanthanides in MYGO and predict the trap depths of $Pr^{3+}$ and $Tb^{3+}$ as 1.68 eV and 1.86 eV, respectively.

### PL and RL in MYGO:Ln

As shown in Fig. 3(a and b), the PLE and PL spectra of MYGO:Pr,Tb were recorded at RT to analyze the optical transition processes of the ions.[33] In Fig. 3(a), the PLE spectrum monitored at 610 nm shows an excitation band at ≈287 nm attributed to IVCT: $Pr^{3+}$ → CB, while the 370–400 nm band is hypothesized to originate from host intrinsic defects. The PLE spectrum monitored at 544 nm shows two excitation bands at ≈276 nm and 320 nm, along with weaker bands in the 350–390 nm range. The strongest excitation band at 276 nm is attributed to IVCT: $Tb^{3+}$ → CB. The most intense excitation band peaked at 276 nm is associated with IVCT: $Tb^{3+}$ → CB. This assignment (IVCT: $Pr^{3+}$/$Tb^{3+}$ → CB) agrees well with the HRBE and VRBE schemes in Fig. 2(e). The excitation band at 320 nm in the

 

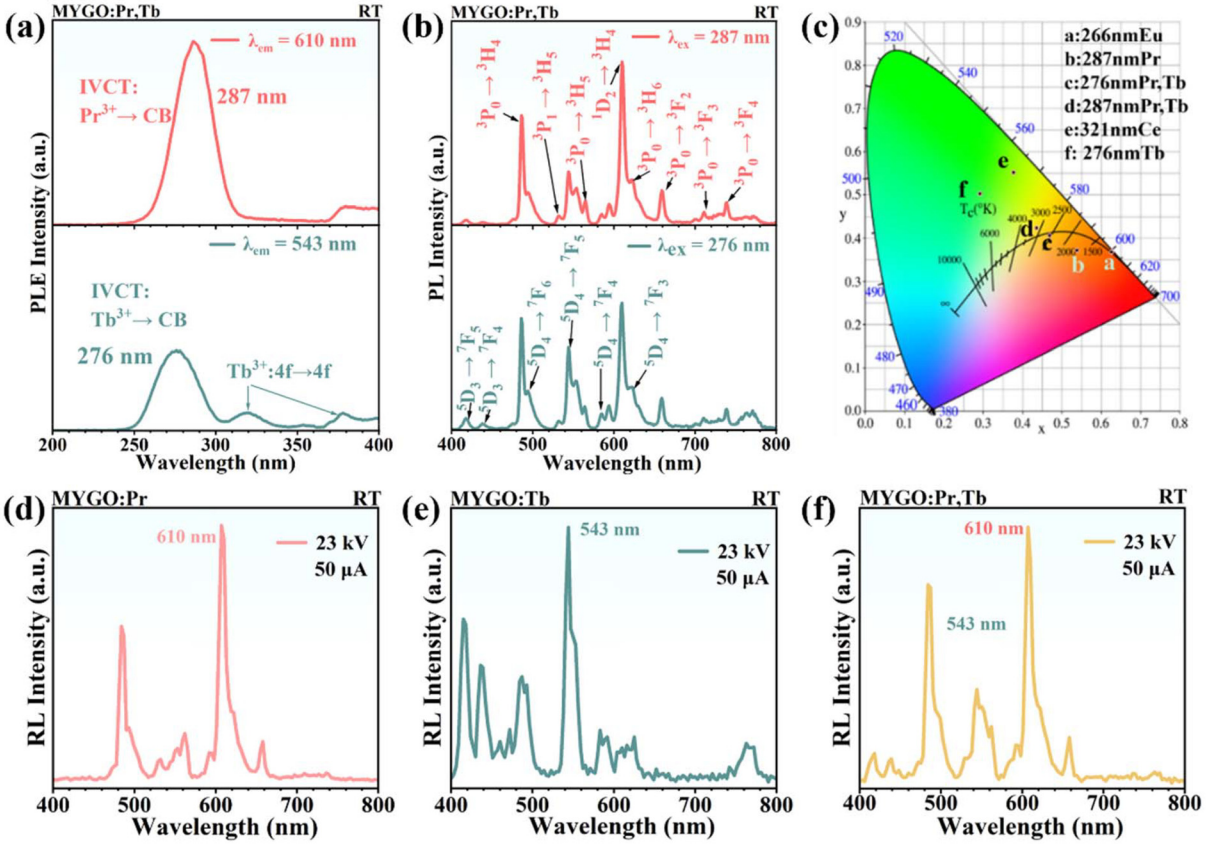


**Fig. 3** (a and b) The PLE (a) and PL (b) spectra of the MYGO:Pr,Tb phosphor monitored at 543/610 nm and 276/286 nm, respectively. (c) The Commission International de l'Éclairage (CIE) color coordinates of MYGO:Ln at different wavelengths of UV irradiation. (d–f) The X-ray RL spectra (*U*/*I* = 23 kV, 50 μA) of the samples MYGO:Pr (d), MYGO:Tb (e) and MYGO:Pr,Tb.

investigated host remains ambiguous, potentially arising from the f–d transitions of $Tb^{3+}$ in a distorted environment or point defects in the material. Excitation bands in the 350–390 nm range are attributed to the spin-forbidden f–f transitions of $Tb^{3+}$. In Fig. 3(b), excitation at 287 nm ($Pr^{3+}$ emissions) reveals several $Pr^{3+}$ 4f–4f transition peaks at 487, 532, 564, 610, 622, 660, 711, and 739 nm, corresponding to transitions $^3P_0 \rightarrow {}^3H_4$, $^3P_1 \rightarrow {}^3H_5$, $^3P_0 \rightarrow {}^3H_5$, $^1D_2 \rightarrow {}^3H_4$, $^3P_0 \rightarrow {}^3H_6$, $^3P_0 \rightarrow {}^3F_2$, $^3P_0 \rightarrow {}^3F_3$, and $^3P_0 \rightarrow {}^3F_4$, respectively. For excitation at 276 nm ($Tb^{3+}$ emissions), the bands correspond to $^5D_3 \rightarrow {}^7F_5$ (417 nm), $^5D_3 \rightarrow {}^7F_4$ (438 nm), $^5D_4 \rightarrow {}^7F_6$ (488 nm), $^5D_4 \rightarrow {}^7F_5$ (544 nm), $^5D_4 \rightarrow {}^7F_4$ (584 nm), and $^5D_4 \rightarrow {}^7F_3$ (619 nm). Fig. 3(b) shows that partial overlap of excitation bands results in PL spectra of co-doped MYGO:Pr,Tb displaying characteristic emission peaks of both $Pr^{3+}$ and $Tb^{3+}$. This indicates that co-doping does not cause fluorescence quenching and achieves dual-luminescence-center emissions. To better evaluate luminescence properties, the PL quantum yields (PLQYs) of MYGO:Ln were measured. Fig. S5† shows that the PLQYs of MYGO:Pr, MYGO:Tb, and MYGO:Pr,Tb are 68.2%, 88.8%, and 71.1%, respectively, indicating that the PL properties of MYGO:Ln are influenced by the type of doping ion. The highest PLQY of 90.4% is achieved with $Tb^{3+}$ doping, confirming the excellent PL properties of MYGO:Tb. Fig. 3(a and b) and Fig. S5† show that the yellow MYGO:Pr,Tb phosphors have PL peaks between 450 nm and 800 nm, with an excitation range below 450 nm, effectively restricting blue light re-absorption. MYGO:Pr,Tb is well matched to blue phosphors excitable by near-UV chips and can be integrated into w-LEDs. Fig. 3(c) presents the CIE color coordinates of the MYGO series at (0.63, 0.37), (0.54, 0.37), (0.47, 0.41), (0.44, 0.42), (0.38, 0.55), and (0.29, 0.50), respectively. This clearly indicates that different PL colors arise from distinct luminescence centers. To assess the feasibility of applying the MYGO series to X-ray multifunctional fields, X-ray RL spectra were recorded. As shown in Fig. 3(d–f), the radioluminescence (RL) spectra of MYGO:Pr (d), MYGO:Tb (e), and MYGO:Pr,Tb (f) closely resemble their respective PL spectra (Fig. S4†). These results demonstrate that MYGO:Ln can be excited by X-rays, with the RL performance closely linked to the luminescence center ions.

### LPL processes in MYGO:Ln

To identify the recombination centers and clarify the LPL decay processes, RT LPL decay spectra were recorded after $U_c$.[22] Fig. 4(a–c) show 2D contour plots of MYGO:Pr (a), MYGO:Tb (b), and MYGO:Pr,Tb (c) for durations of 120, 60, and

15 min, respectively. The LPL spectra of MYGO:Pr and MYGO:Tb, ranging from 400 to 800 nm, exhibit similar trends, with the LPL intensity decreasing over time. For MYGO:Pr,Tb, the LPL decay spectra, resembling the PL spectra, primarily consist of $Pr^{3+}$: $^3P_0 \rightarrow {}^3H_4$, $^3H_6$ and $Tb^{3+}$: $^5D_3$, $^5D_4 \rightarrow {}^7F_j$ transitions. In Fig. 4(a), the LPL decay curves for $Pr^{3+}$: $^3P_0 \rightarrow {}^3H_4$, $^3H_6$ emissions at 487 and 610 nm exhibit a rapid initial decay within 20 min, followed by a slower decrease. In Fig. 4(b), the LPL decay curves for $Tb^{3+}$: $^5D_4 \rightarrow {}^7F_5$ emission ($\lambda_{em}$ = 543 nm) show low initial intensity and rapid decay. In Fig. 4(c), the decay curves at 487, 543, and 610 nm for MYGO:Pr,Tb indicate that $Pr^{3+}$ has a higher LPL intensity than $Tb^{3+}$, and both ions serve as LPL and recombination centers. As shown in Fig. 3(d), the initial intensity after $U_c$ exceeded 100 mcd $m^{-2}$, and the $\tau_p$, $\tau_t$, and $\tau_c$ values were approximately 405, 179, and 48 min, respectively, demonstrating excellent luminescence performance for MYGO:Ln. To study electron and hole trapping and release processes, RT isothermal LPLE spectra of MYGO:Pr,Tb (monitored at 487, 543, and 610 nm) were recorded after 200–400 nm photon charging, as shown in Fig. 4(e–g). In Fig. 4(h), the LPLE plots of MYGO:Pr,Tb are similar to the PLE spectra but exhibit a blue shift. This indicates that the LPL of MYGO:Pr,Tb phosphors is driven by IVCT: $Pr^{3+}/Tb^{3+} \rightarrow$ CB. Notably, no intrinsic defect bands appear in the LPLE spectra, indicating that intrinsic defect generation is not involved in the LPL processes.

### PSL processes in MYGO:Ln

Photo-stimulated luminescence (PSL) is a phenomenon where low-energy light stimulates materials excited by high-energy light to emit luminescence.[22] It is widely applied in advanced optical storage technologies. Some charge carriers trapped in the material cannot be activated at RT. Stored carriers can be released through low-energy photo-stimulation. Deep traps in PSL materials prevent information loss. In other words, PSL phenomena can qualitatively predict information storage properties. Therefore, MYGO:Pr,Tb was investigated as a PSL research object to explore the possibility of containing independent deep traps, as shown in Fig. 5(a–d). Real-time PSL curves were recorded after $U_c$. The 808 nm and 980 nm NIR lasers were alternately turned "on" and "off" every 30 s for 30 min, causing alternating jumps and drops in PSL intensity. This indicates that electrons in deep traps cannot be fully cleared by thermal perturbation at RT but are effectively excited by NIR stimulation. For MYGO:Pr,Tb, the 808 nm and 980 nm NIR PSL (PSL-808, PSL-980) enable partially responsive optical information readout with a high response rate. These results suggest that MYGO:Pr,Tb can enable multi-mode anti-counterfeiting applications, including PL, LPL, and NIR PSL. As shown in Fig. 5(e), the X-ray storage performance of MYGO was quantified by comparing the TL curves of MYGO:Ln with commercial phosphors $SrAl_2O_4:Eu^{2+},Dy^{3+}$ and $BaFBr(I):Eu^{2+}$ after $X_c$. For MYGO:Ln, the peak temperature of the TL band ($T_m$) shifted to higher values, with TL intensity ratios of 1.298/1.228 ($r_1/r_4$), 0.504/0.477 ($r_2/r_5$), and 1.517/1.435 ($r_3/r_6$), respectively. To explore anti-counterfeiting applications, TL curves ($X_c$) of MYGO:Pr,Tb with varying durations were analyzed. As shown in Fig. 5(f), the TL intensity increased with $X_c$ time, and TL peaks shifted to the right. The inset of Fig. 5(f) shows that the integrated TL intensity fits the equation TL × $10^{-8}$ = 2.002 × $t$ − 0.422 ($R^2$ = 0.9996), where $t$ represents the X-ray charging time. This suggests that MYGO:Pr,Tb storage phosphors are promising candidates for X-ray detection dosimeters.

### TL curves and trap depths of MYGO:Ln

To determine the trap depths of MYGO:Ln and validate the VRBE and HRBE models, we systematically studied and recorded their TL curves. Fig. 6(a–c) show the TL curves of MYGO:Ln (310–650 K) after $X_c$ at heating rates ($\beta$) ranging from 0.3 to 1.5 K $s^{-1}$. As $\beta$ increased, the TL intensity ($I_{TL}$) of MYGO:Ln strengthened, and $T_m$ shifted to higher temperatures. To analyze the recombination and luminescence centers during TL decay, TL curves of MYGO:Ln at $\beta$ = 1 K $s^{-1}$ in Fig. 6(d) were Gaussian fitted and compared. The fitting parameters for TL curves are listed in Tables S5–7.† In Fig. 6(d1) and (d3), $T_m$ for MYGO:Tb ($T_m$-Tb) is higher than that for MYGO:Pr ($T_m$-Pr). In Fig. 6(d3), $I_{TL}$ for MYGO:Pr ($I_{TL}$-Pr) is approximately 2.5 times that of MYGO:Tb ($I_{TL}$-Tb). These bands are speculated to originate from unknown intrinsic defects, impurities, or $Ln^{3+}$. To better understand the type and depth of traps, Gaussian-fitted curves of MYGO:Ln in Fig. 6(d) and Fig. S6–8† were analyzed. TL curves of MYGO:Pr [Fig. 6(d3), Fig. S6†] and MYGO:Tb [Fig. 6(d1), Fig. S7†] each contain four fitted TL peaks. Fitted TL bands 1–3 of MYGO:Pr and MYGO:Tb share similar shapes and $T_m$ values (≈380, 420, and 490 K). Therefore, The TL fitted curves of MYGO:Pr and MYGO:Tb are divided into two parts: low-temperature bands 1–3 (bands H) and high-temperature bands 4 (band P, $T_m$ = 549 K in MYGO:Pr) and 5 (band T, $T_m$ = 569 K in MYGO:Tb). Bands H, P and T correspond to host-induced traps (intrinsic defects), $Pr^{3+}$-induced defects, and $Tb^{3+}$-induced defects, respectively. For MYGO:Pr,Tb, five TL fitted peaks are shown in Fig. 6(d2) and Fig. S8.† The low-temperature bands 1–3 ($T_m \approx$ 382 K, 427 K, 489 K) are similar to the bands H of MYGO:Pr and MYGO:Tb, while the high-temperature bands 4 ($T_m \approx$ 543 K) and 5 ($T_m \approx$ 581 K) resemble band P ($T_m \approx$ 549 K) of MYGO:Pr and band T ($T_m \approx$ 569 K) of MYGO:Tb, respectively. Thus, the Gaussian-fitted TL curves of MYGO:Pr,Tb can be divided into three parts: bands H (1–3), band P (4), and band T (5). Therefore, the TL curves of MYGO:Ln comprise bands H, P, and T, corresponding to host intrinsic defects, $Pr^{3+}$ traps, and $Tb^{3+}$ traps, respectively. Fig. 6(e–h) display TL bands P for MYGO:Pr, bands T for MYGO:Tb, and bands P and T ($P_c$, $T_c$) for MYGO:Pr,Tb after $X_c$. Source data are provided in Fig. S6–8.† Finally, trap depths were estimated using formula (4) and the variable $\beta$ rate profiles of TL bands P, T, $P_c$ and $T_c$ in Fig. 6(e–h):

$$\beta E/(k_B T_m^2) = s \times \exp(-E/k_B T_m) \quad (4)$$

 

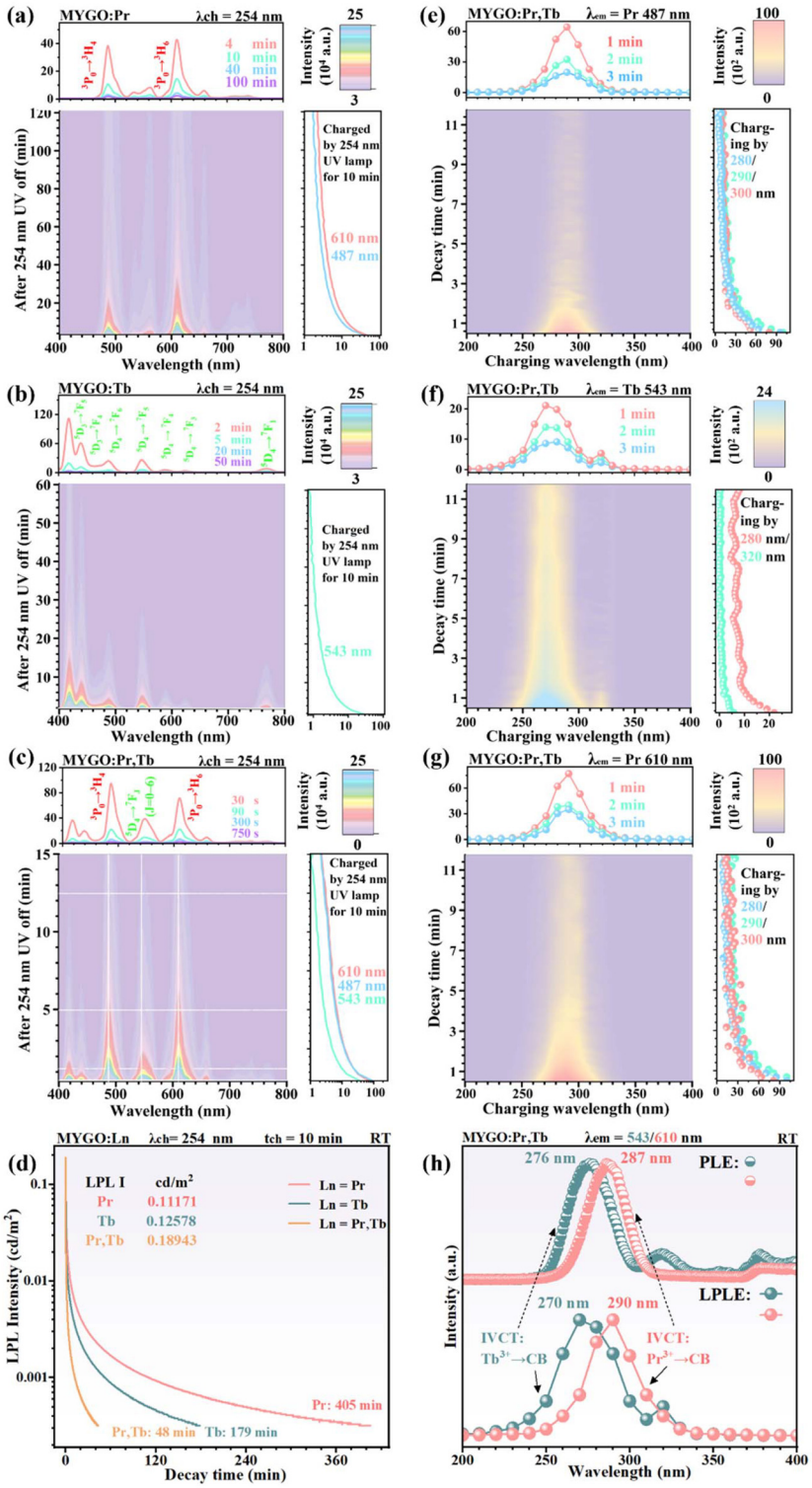


**Fig. 4** (a–c) The RT isothermal LPL spectra of the materials MYGO:Pr (a), MYGO:Tb (b), and MYGO:Pr,Tb (c) after 254 nm UV lamp charging for 10 min. (d) The LPL decay curves of MYGO:Ln after charging with a 254 nm UV lamp for 10 min. (e–g) The RT isothermal decay curves of MYGO:Pr, Tb monitored at 487 (e), 543 (f), and 610 (g) nm after different energy photon excitation for 10 min. (h) The comparison of LPL excitation (LPLE) curves with the PLE spectra of MYGO:Pr,Tb.

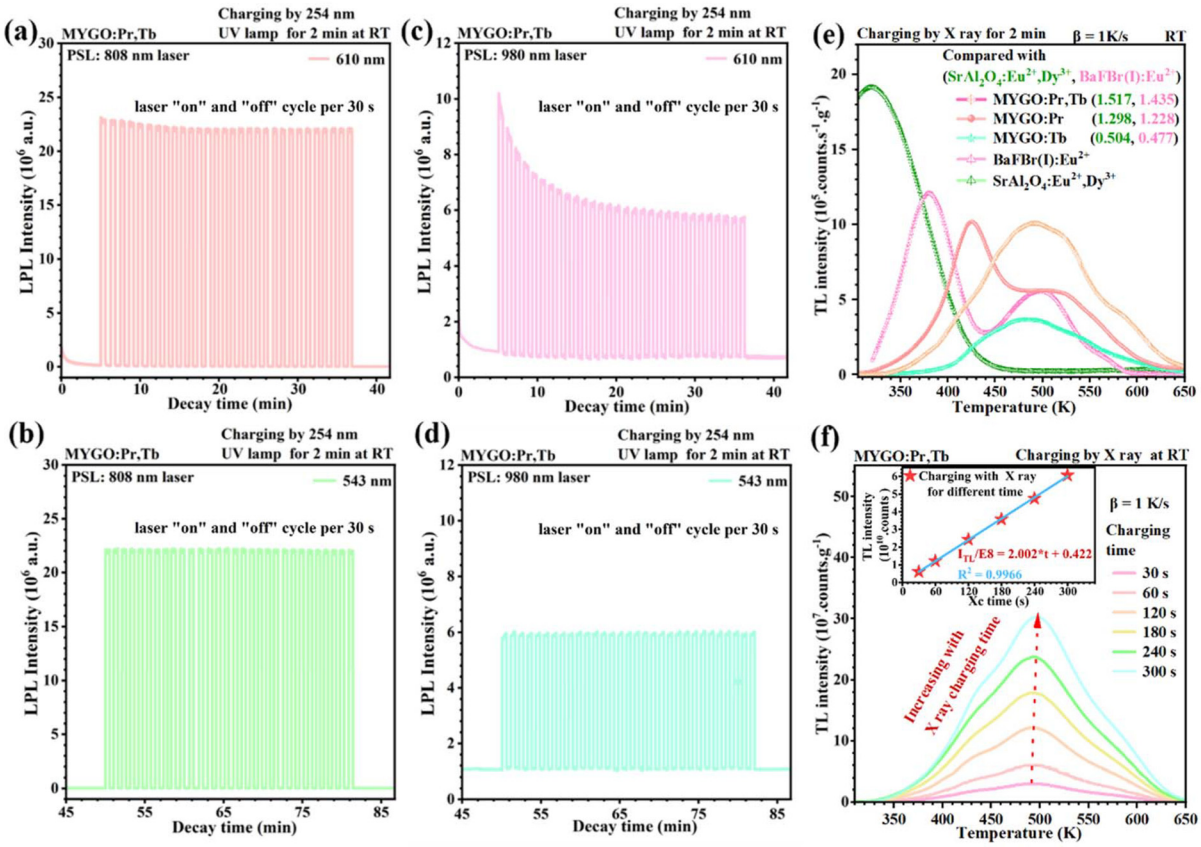


**Fig. 5** (a–d) After the recharged MYGO:Pr,Tb decayed in the dark, PSL cycle decay curves monitored at 610 nm (a) and 487 nm (b) under an 808 nm NIR laser and at 610 nm (c) and 487 nm (d) under a 980 nm NIR laser were recorded in pulsed mode (repeating ON and OFF in every 30 s) at RT. (e) The comparison of TL curves for MYGO:Ln and commercial phosphors $SrAl_2O_4:Eu^{2+},Dy^{3+}$/BaFBr(I):$Eu^{2+}$ charged by X-rays for 2 min. (f) The TL curves of MYGO:Pr,Tb charged by X-rays for different durations. The inset shows the integrated TL intensities between 310 and 650 K as a function of X-ray exposure time.

Here, $\beta$ (K $s^{-1}$) is the heating rate, $E$ (eV) is the trap depth, $k_B$ is the Boltzmann constant, $T_m$ (K) is the TL peak temperature, and $s$ ($s^{-1}$) is the frequency factor. By plotting ln ($T_m^2$) against 1/($k_B \times T_m$), straight lines representing trap depths $E$ (slopes) and frequency factors $s$ are shown in Fig. 6(j) and Table S9.† In Fig. 6(j), fitted lines from the same traps are parallel and exhibit consistent trap depths $E$. Trap depths $E$ for bands P, T, $P_c$ and $T_c$ are calculated as 1.668, 1.684, 1.867, and 1.798 eV, respectively. Based on Fig. 6, $Tb^{3+}$ co-doping generates new hole traps and increases trap depths, while $Pr^{3+}$ co-doping enhances the TL intensity *via* Coulomb interactions. Altogether, $Pr^{3+}$ and $Tb^{3+}$ co-doping improves the luminescence performance through higher TL intensity and greater trap depths. Notably, the trap depths agree well with the energy differences between 4f-$Pr^{3+}$/$Tb^{3+}$ and the VB top in the VRBE and HRBE schemes. Consequently, we identified a trap depth engineering strategy for MYGO and successfully developed novel deep-trap LPL and X-ray storage materials.

### Charge carrier trapping and release processes in MYGO garnet

Higher initial storage capacity and lower release rates are critical for superior storage material performance. The integral area percentage ($I_{TL}$) and $T_m$ of TL curves represent carrier storage capacity and release rates. TL curves of MYGO:Ln (310–650 K) were investigated after $U_c$ or $X_c$ for 2 min to quantify the storage capacity in the temperature-cleaning ($t_{clean}$) or decay time ($t_d$) dimensions. Fig. 7 shows that $I_{TL}$ gradually decreases and $T_m$ shifts to higher temperatures with increasing $t_{clean}$ or $t_d$. In the $t_d$ dimension, Fig. 7(a and b) illustrate TL curve trends for MYGO:Pr (a) and MYGO:Tb (b) as $t_d$ increases (0 s–120 h) after $U_c$. The $I_{TL}$ ratio of MYGO:Pr to MYGO:Tb at 0 s is 1.5, indicating that MYGO:Pr has higher initial storage capacity. Compared to $T_m$-Pr (≈386 K), $T_m$-Tb (≈417 K) indicates deeper trap depths in MYGO:Tb. In Fig. 7(a and b), MYGO:Tb retains 49% of carriers at $t_d$ = 120 h, demonstrating a lower release rate and reduced RT thermal perturbation. Fig. 7(c) shows that MYGO:Pr,Tb retains high initial $I_{TL}$, $T_m$ (≈418 K), and 50% of carriers at $t_d$ = 120 h, combining the high storage capacity of MYGO:Pr and low release rate of MYGO:Tb. The type of charging energy significantly affects the storage capacity. In Fig. 7(d–f), $I_{TL}$ after $X_c$ decreases by an order of magnitude compared to $U_c$, but $T_m$ increases to 425 K (d), 483 K (e), and 493 K (f), indicating that carriers shift to deeper traps with lower release rates. For MYGO:Pr,Tb, half of the carriers are released after 100 h ($X_c$) or 1000 h ($U_c$).

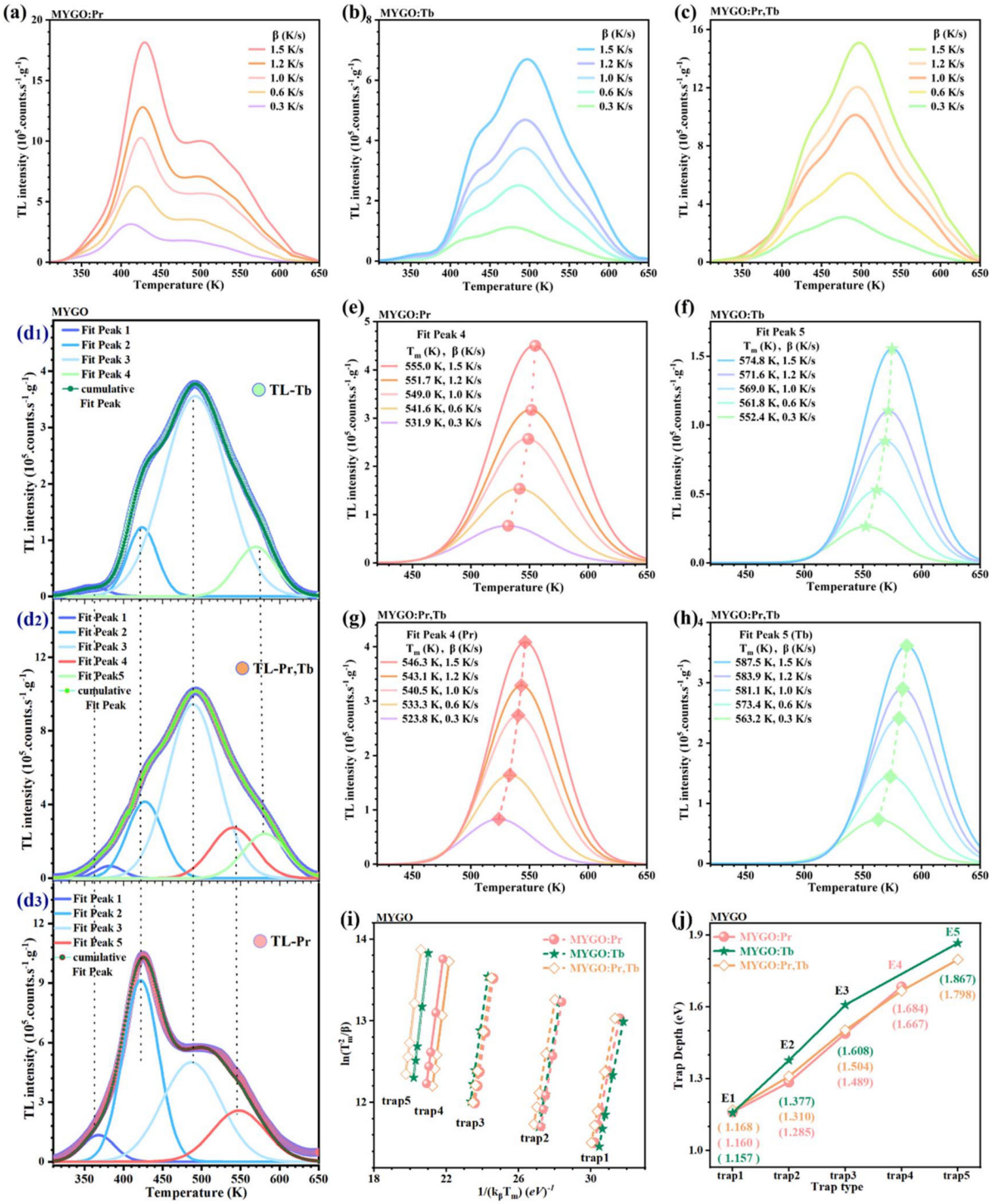


**Fig. 6** (a–c) The TL curves of the materials MYGO:Pr (a), MYGO:Tb (b), and MYGO:Pr,Tb (c), charged with X-rays for 2 min, recorded at varying heating rates ($0.3 \leq \beta \leq 1.5$ K $s^{-1}$). (d) Fitting TL curves for bands H (Fit Peaks 1, 2, 3), P (Fit Peak 4), and T (Fit Peak 5) in MYGO:Tb (d1), MYGO:Pr,Tb (d2) and MYGO:Pr (d3) at $\beta = 1$ K $s^{-1}$. (e–h) The TL curves of bands P (Fit Peak 4) in MYGO:Pr (e), bands T (Fit Peak 5) in MYGO:Tb (f), and Fit Peak 4 in MYGO:Pr (g) and MYGO:Pr,Tb (h) at varying heating rates ($0.3 \leq \beta \leq 1.5$ K $s^{-1}$). (i) The heating rate plots of MYGO:Ln. (j) The trap depth plots of MYGO:Ln.

Therefore, Fig. 7(a–f) illustrate that $Pr^{3+}$ and $Tb^{3+}$ co-doping in MYGO enhances the storage performance compared to single doping in the $t_d$ dimension. And X-rays are more suitable for long-term storage applications, while 254 nm UV is better for large-capacity storage. In the $t_{clean}$ dimension, storage performance was evaluated by uniformly

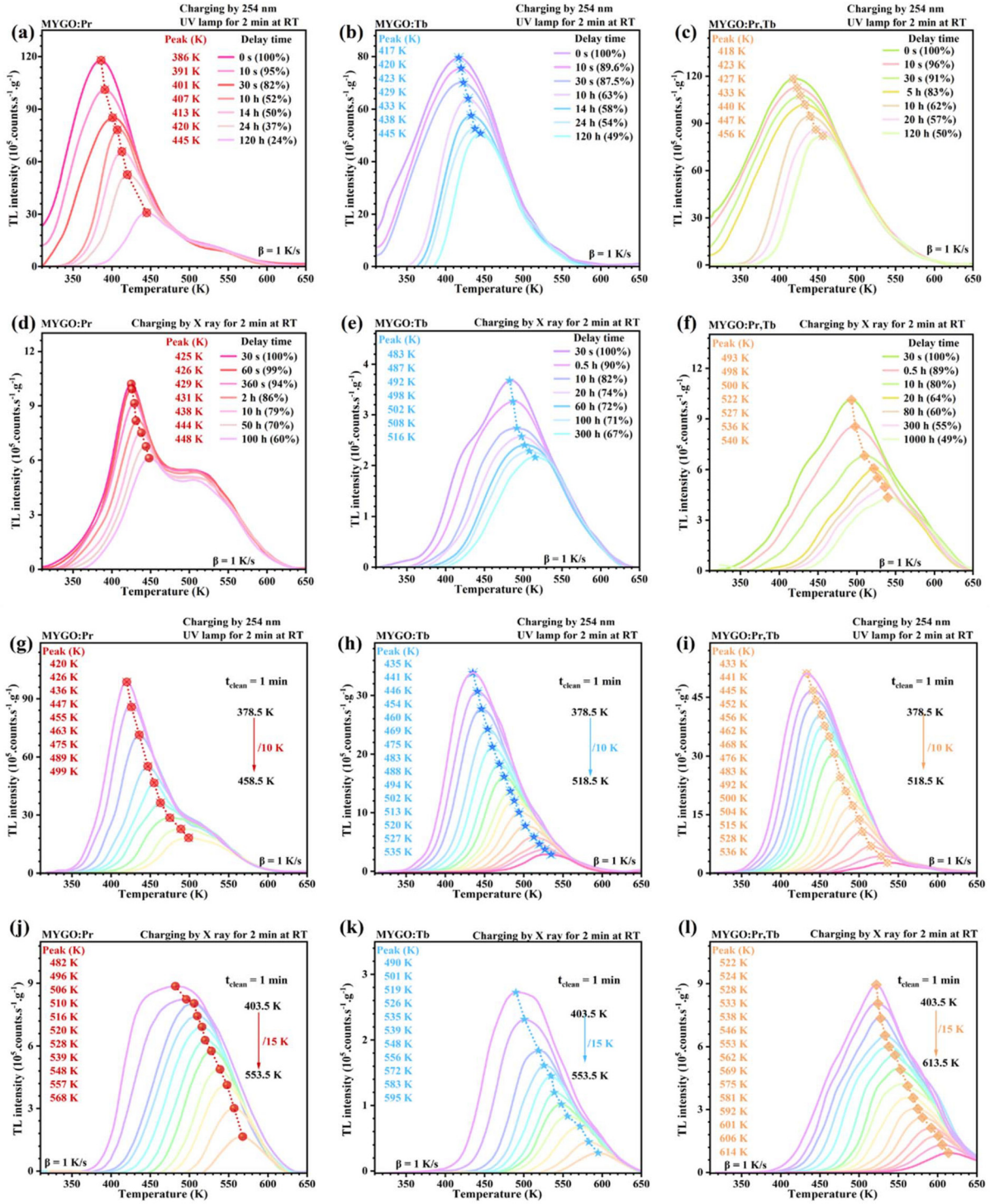


**Fig. 7** (a–c) Fading of TL curves of MYGO:Pr (a), MYGO:Tb (b), and MYGO:Pr,Tb (c) after charging with a 254 nm UV lamp, with different delay times. (d–f) Fading of TL curves of MYGO:Pr (d), MYGO:Tb (e), and MYGO:Pr,Tb (f) after charging with X-rays for 2 min, with different delay times. (g–i) TL glow curves for MYGO:Pr (g), MYGO:Tb (h), and MYGO:Pr,Tb (i) recorded at $\beta$ = 1 K $s^{-1}$ after charging with a 254 nm UV lamp, followed by TL glow peak cleaning at $t_{clean}$ for 1 min. (j–l) TL glow curves for MYGO:Pr (j), MYGO:Tb (k), and MYGO:Pr,Tb (l) recorded at $\beta$ = 1 K $s^{-1}$ after X-ray charging, followed by TL glow peak cleaning at $t_{clean}$ for 1 min.

increasing $t_{clean}$. Fig. 7(g–l) show that $T_m$ shifted to higher temperatures after $X_c$ (g–i) or $U_c$ (j–l) for MYGO:Ln. The TL curves for $t_{clean}$ and $t_d$ yielded similar results, showing that MYGO:Pr (g and j), MYGO:Tb (h and k), and MYGO:Pr,Tb (i and l) exhibit higher initial storage capacity, lower release rates, or both. Fig. 7(g–i) show that after $U_c$ and increasing

 

$t_{clean}$, carrier release is the fastest in MYGO:Pr (j) but slower and more gradual in MYGO:Tb (h) and MYGO:Pr,Tb (i). The initial $t_{clean}$ ($X_c$) was raised to 403 K. In Fig. 7(j and k), as $t_{clean}$ increases from 403.5 K to 553.5 K, stored carriers are slowly released, and $T_m$ shifts to 482 K (MYGO:Pr) or 495 K (MYGO:Tb). For MYGO:Pr,Tb (i and l), major carrier release requires $T_m$ to exceed 518.5 K ($U_c$) or 613.5 K ($X_c$). Fig. 7 confirms that MYGO:Ln, especially MYGO:Pr,Tb, is a novel deep-trap X-ray storage material with excellent storage performance.

## Applications

**X-ray imaging of MYGO:Ln.** Fig. 8(a1) shows MYGO:Pr, MYGO:Tb, and MYGO:Pr,Tb storage phosphors dispersed in PDMS to form films 1–3, each with a diameter of ≈8 cm. No PL is visible under daylight, as shown in Fig. 8(a1), but under 254 nm UV light, as shown in Fig. 8(a2), films 1–3 emit pink, green, and yellow PL, respectively. For X-ray imaging, the films were placed under four large wire connectors (Fig. S9†), exposed to 75 W X-rays, and then heated to ≈400 K after removing the connectors, emitting TSL in the dark to produce



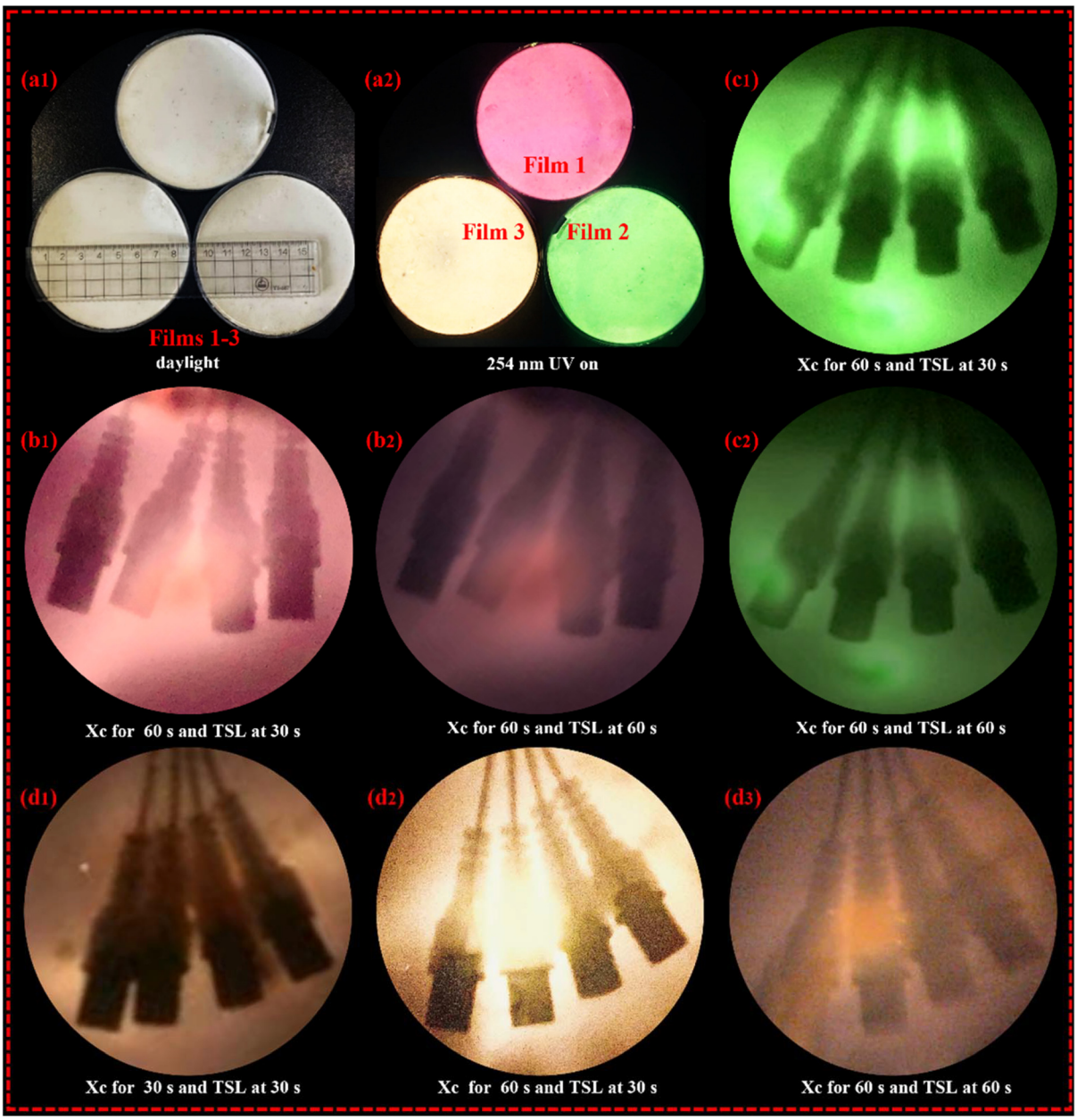


**Fig. 8** Proof-of-concept planar X-ray imaging using MYGO-based PDMS film 1 (MYGO:Pr), film 2 (MYGO:Tb), and film 3 (MYGO:Pr,Tb). (a) The photographs of films 1, 2, and 3 under daylight (a1) and under a 254 nm UV lamp (a2). (b–d) The TSL X-ray imaging photographs of four electronic connectors in film 1 (b), film 2 (c), and film 3 (d).

X-ray imaging photographs. Fig. 8(b1, b2) and (c1, c2) show that film 1 and film 2 emit pink and green TSL, respectively, originating from the 4f–4f transitions of $Pr^{3+}$ and $Tb^{3+}$. Fig. 8 (d1–d3) reveal that film 3 emits orange TSL, combining pink $Pr^{3+}$ and green $Tb^{3+}$ emissions. Fig. 8(b1, c1 and d2) present X-ray imaging photographs after 60 s $X_c$ and 30 s heating. The brightness and clarity are in the order: film 3 > film 1 > film 2, indicating that MYGO:Pr,Tb has the best X-ray imaging capability. As shown in Fig. 8(b2, c2 and d3), extending the heating time from 30 s to 60 s reduces brightness and clarity due to significant carrier release. X-ray imaging photographs of film 2 show poor definition due to the lowest storage capacity of MYGO:Tb and insufficient heating temperature to reach $T_m$. Fig. 8(d1 and d2) show that for film 3, brightness and clarity are proportional to $X_c$ time. Overall, Fig. 8 illustrates the excellent X-ray imaging properties of MYGO:Ln materials, particularly MYGO:Pr,Tb phosphors.

**Anti-counterfeiting and encryption.** Fig. 9(a) displays the type and distribution of MYGO series phosphors in the 3D-printed digital model '8 8 8 8'. Under 365 nm UV irradiation, the MYGO series phosphors emit weak PL, and the digital model displays the original information '8 8 8 8' (Fig. 9(b1)). When 254 nm UV light is turned on (Fig. 9(b2)), all MYGO series except for MYGO:Ce emit bright PL, revealing the transformed information '6 8 9 9'. After $U_c$, the digital model emits LPL and is used to demonstrate encryption and anti-counterfeiting. At 5 s (Fig. 9(b3)), the LPL image displays '5 0 9 3', as all MYGO series except for MYGO:Ce and MYGO:Eu emit LPL. Then, at 60 s (Fig. 9(b4)), due to differing LPL durations, only MYGO:Pr,Tb has completely decayed, transforming the information from '5 0 9 3' to '5 0 5 1'. Finally, at 120 s (Fig. 9(b5)), only MYGO:Pr emits visible LPL, changing the information from '5 0 5 1' to '5 0 5' or 'S O S'. After 24 h decay in the dark and heating to 373 K, the information '5 0 9 3' reappears brightly and clearly (Fig. 9(b6)). This phenomenon of combining PL, LPL, and TSL to display different information has great prospects for applications in anti-counterfeiting and advanced displays.

**Information storage.** Fig. 9(c) shows 3D-printed QR code models containing the information '$Mg_3Y_2Ge_3O_{12}:Pr^{3+}$, $Tb^{3+}$'. MYGO:Pr, MYGO:Tb, and MYGO:Pr,Tb storage phosphors were dispersed in PDMS and incorporated into QR code models to create QR codes 1, 2, and 3. Under 254 nm UV light, QR codes 1, 2, and 3 emit bright pink, green, and orange PL, as displayed in Fig. 9(d1, e1 and f1), respectively. These QR codes were used to evaluate LPL properties after $U_c$. As shown in Fig. 9(d2, e2 and f2), LPL images at 5 s confirm that the information '$Mg_3Y_2Ge_3O_{12}:Pr^{3+}$,$Tb^{3+}$' is embedded in the QR codes. In Fig. 9(d3, e3 and f3), LPL images at 120 s, 60 s, and 30 s for QR codes 1, 2, and 3, respectively, show slight fading. Fig. 9(d4, e4 and f4) show that after 24 h decay in the dark and heating to 372.5 K for 30 s, carrier release is accel-

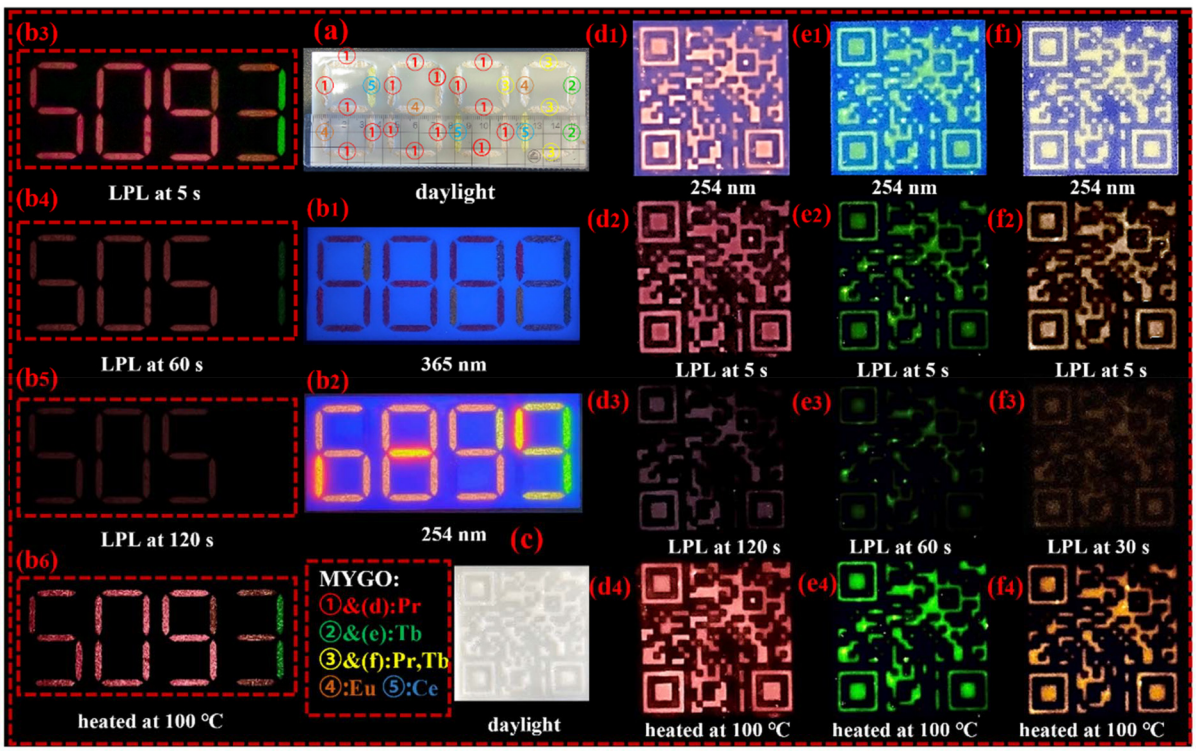


**Fig. 9** The proof-of-concept images for anti-counterfeiting and information storage applications using the MYGO-based PDMS QR code 1 (MYGO:Pr), QR code 2 (MYGO:Tb), and QR code 3 (MYGO:Pr,Tb). (a and b) The photographs of anti-counterfeiting features of the digital model "8 8 8 8". (c) The QR code models in daylight. (d–f) The information storage photographs for QR code 1 (d), QR code 2 (e), and QR code 3 (f).

 

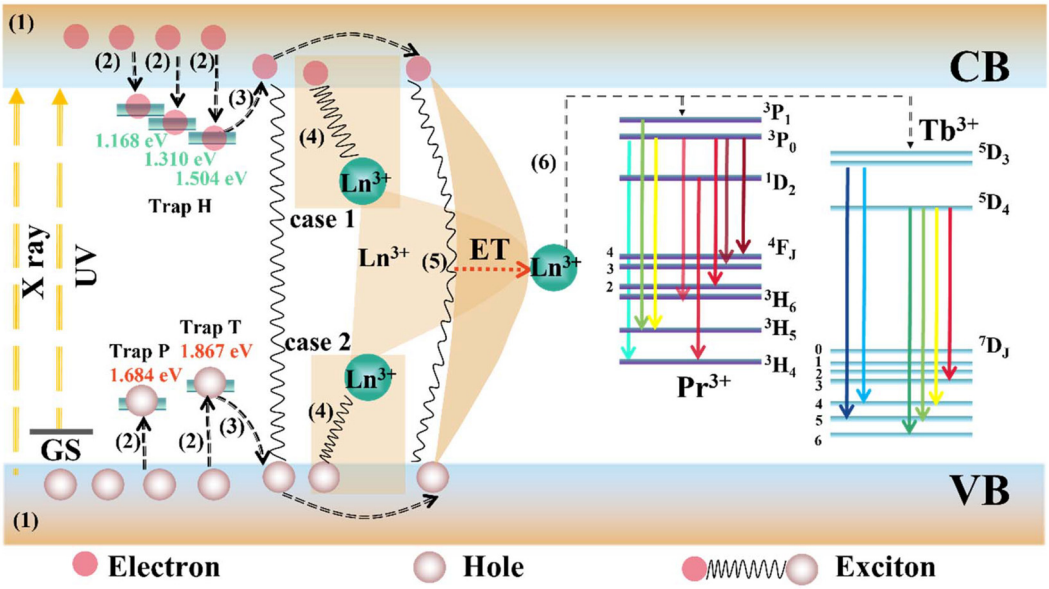


Fig. 10 The schematic illustration of the LPL mechanism of the MYGO:Pr,Tb phosphor depending on the VRBE and HRBE models.

erated, producing high-brightness TSL. Notably, TSL images are brighter and clearer than LPL images, confirming that the MYGO:Ln series are excellent information storage materials.

### Mechanism of LPL

Above all, the possible LPL mechanism in MYGO:Ln is proposed and illustrated in Fig. 10. Under 254 nm UV or X-ray charging, electrons in the VB are excited to the CB, leaving behind numerous holes in the VB (1). Some electrons immediately return to the ground state, producing direct PL from $Pr^{3+}$ or $Tb^{3+}$. Simultaneously, holes in the VB or electrons in the CB are trapped by hole traps ($Ln^{3+}$: $Pr^{3+}$ and/or $Tb^{3+}$) or electron traps (MYGO host), respectively (2). After the excitation ceases, trapped electrons and holes are released into the CB and VB, respectively, under thermal interference at RT (LPL) or additional energy stimulation, *e.g.* TSL or PSL (3). $Ln^{3+}$ (case 1 or 2) first attracts an electron or a hole (4) and subsequently attracts a hole or an electron, forming an exciton under Coulomb force. Alternatively, released electrons and holes directly recombine to form excitons, which migrate through the lattice and are eventually captured by $Ln^{3+}$ (5). In all cases, $Ln^{3+}$ binds to excitons, acquires their recombination energy, and transitions to the excited state (6). After non-radiative relaxation, LPL arises from the 4f → 4f transition of $Ln^{3+}$.

## 3. Conclusions

In this work, $Mg_3Y_2Ge_3O_{12}$ (MYGO) series LPL materials were synthesized using a high-temperature solid-phase method. Combining the refined chemical shift model, optical spectroscopy, and TL curves, the HRBE and VRBE schemes for MYGO materials were constructed and validated, predicting trap depths of $Pr^{3+}$ and $Tb^{3+}$ as 1.68 eV and 1.86 eV, respectively. Experimental trap depths calculated from $X_c$ TL curves matched the predictions. Lanthanide ions ($Pr^{3+}$ and/or $Tb^{3+}$) act as deep hole traps, while host intrinsic defects serve as electron traps. LPL decay curves demonstrate excellent performance of the MYGO series, with initial intensities exceeding 100 mcd $m^{-2}$ and $\tau_p$, $\tau_t$, and $\tau_c$ measured as 405, 179, and 48 min, respectively. The red LPL phosphor MYGO:Pr offers a significant advantage, as most lanthanide-activated LPL materials last less than 6 h. As a novel yellow LPL phosphor, MYGO:Pr,Tb emits across 400–800 nm with an excitation range below 400 nm, addressing issues like blue light re-absorption and insufficient red components, which affect color rendering and white light uniformity. Regarding storage ability, 49% of carriers in MYGO:Pr,Tb can be retained over 1000 h.

TL intensity ratios for MYGO:Pr, MYGO:Tb, and MYGO:Pr,Tb compared to commercial $SrAl_2O_4:Eu^{2+},Dy^{3+}$/BaFBr(I):$Eu^{2+}$ are 1.298/1.228 ($r_1/r_4$), 0.504/0.477 ($r_2/r_5$), and 1.517/1.435 ($r_3/r_6$), respectively. Based on the LPL mechanism model, the processes of energy level transitions at the luminescence center, as well as the storage and release of carriers, have been elucidated. Finally, the MYGO series demonstrates multifunctional applications in anti-counterfeiting, information storage, and X-ray imaging through PL, LPL, TL, and TSL. Above all, MYGO:Pr,Tb has the prospects of being matched well with blue phosphors and used for w-LED applications, and the MYGO series can be an excellent candidate for multifunctional applications in LPL, anti-counterfeiting, advanced displays, high-capacity storage and X-ray imaging. This study offers a theoretical framework and experimental methodology for designing novel LPL and storage phosphors.

# 4. Experimental section

### Materials and synthesis

According to the stoichiometric ratio, the raw materials MgO (99.99%), $Y_2O_3$ (99.99%), $GeO_2$ (99.99%), $Pr_7O_{11}$ (99.99%), $Tb_2O_3$ (99.99%), $CeO_2$ (99.99%), and $Eu_2O_3$ (99.99%) were added to an agate mortar. Then, an appropriate amount of absolute ethanol was poured in and the mixture was ground for 0.5 h. The detailed compositions are listed in Table S1.† The mixture was calcined in a high-temperature tube furnace at 1623 K for 6 h in a muffle furnace under air, finally cooled to room temperature (RT), and the temperature rate of rise and fall obtained was 5 K $min^{-1}$.

### Device preparation

**Application in information storage.** Three 2D code models (60 × 60 × 4 mm) containing the information '$Mg_3Y_2Ge_3O_{12}$:$Pr^{3+}$,$Tb^{3+}$' were printed using the ASM 360 light-curing SLA 3D printer (manufactured by Dongguan Ansam Intelligence Co.). 1.5 g each of MYGO:Pr, MYGO:Tb, and MYGO:Pr,Tb and 1.5 g of polydimethylsiloxane (PDMS, The Dow Chemical Company) precursors were mixed with constant stirring in three Petri dishes with a diameter of 80 mm. Then, the mixtures were poured into the QR code moulds, uniformly distributed, and baked in a vacuum oven at 343 K for 12 h. 254 nm UV light was used to energize the QR codes before LPL experiments.

**Anti-counterfeiting and encryption applications.** MYGO:Ce, MYGO:Eu, MYGO:Pr, MYGO:Tb, and MYGO:Pr,Tb were filled into different parts of the digital model '8 8 8 8' printed using a 3D printer. After exposing all the models to 254 nm UV light for 10 min, the LPL-induced changes in character patterns on the surface were recorded.

**X-ray imaging.** 3 g of MYGO:Pr, MYGO:Tb, and MYGO:Pr, Tb storage phosphors were each dispersed in PDMS and subsequently baked in a vacuum oven at 343 K for 12 h to synthesize three flexible films 1–3 with a diameter of ≈8 cm. Films 1–3 were placed under four large wire connectors after being irradiated with an X-ray radiation source for different times. The wire connectors were removed. The X-ray charged films 1–3 were heated to ≈400 K in the dark using a heater, and a series of X-ray imaging photographs were taken.

**Characterization and measurements.** In this work, X-ray diffraction (XRD) measurements were performed with the following parameters: voltage $U$ = 40 kV, current $I$ = 60 mA, CuKα (with a wavelength ($\lambda$) of 1.54178 Å) as the X-ray source, a scanning step of 0.03°, and a scanning speed of 10° $min^{-1}$, over a range of 10–90°. When the diffraction patterns of the samples are refined through GSAS software, the scanning step is adjusted to 0.01°, the scanning speed is reduced to 1.5° $min^{-1}$, and other parameters remain unchanged. The surface morphology (SEM) and elemental distribution (EDS) of the MYGO host and MYGO:Ln phosphors were measured using a Hitachi S-4800 scanning electron microscope. UV-visible diffuse reflectance spectra (UVV-DRS) of MYGO:Ln were recorded using a spectrophotometer (Shimadzu, SOLID 3600) equipped with a $BaSO_4$-based integrating sphere at room temperature (RT). The LPL decay curves were obtained using the PR305 instrument produced by Zheda Tricolor Instrument Co., Ltd. The light source was a 254 nm UV lamp with an illumination of 1000 Lx, and the irradiation time was 10 min. The PL excitation (PLE), PL, LPL excitation (LPLE), LPL spectra and photo-stimulated luminescence (PSL) spectra were recorded using an FLS920T-VM504 vacuum UV-visible (UVV) test system and a Flurolog-3 spectrometer system (HORIBA JOBIN YVON). A xenon lamp was used as the light source for the PLE and PL spectra, whereas the LPLE, LPL and PSL spectra were recorded using only an 808 nm or 980 nm NIR laser (both 0.3 W power) source after 2 min of $U_c$. A miniaturized X-ray tube (Amptek) with a maximum output of 4 W was employed as the X-ray source. Radioluminescence (RL) was acquired with an integrating sphere ($\Phi$ = 10 cm) and a fiber-optic spectrometer (Omni-λ300i). For RL measurement under X-ray irradiation, the X-ray tube voltage and current were kept at 23 kV and 100 μA, respectively. The FJ427A1 microcomputer thermoluminescence dosimeter produced by Beijing Nuclear Instrument Factory was used to record the TL curves. 5 mg samples were measured within the range of 310–650 K at heating rates ($\beta$) of 0.3, 0.6, 0.9, 1.2 and 1.5 K $s^{-1}$. A silver-targeted X-ray tube with a power of 2.3 W ($I$ = 100 μA, $U$ = 23 kV) or a 254 nm UV lamp was used for charging for 2 min prior to TL curve measurement. An industrial X-ray tube operating at 75 W ($U$ = 50 kV and $I$ = 1.5 mA) was employed as the energy source for X-ray imaging, with the distance between the X-ray tube and the LPL films being about 80 mm. Prior to TL, LPL, and PSL measurement, the samples were irradiated under a 254 nm UV lamp for 10 min, unless stated otherwise. The power of the 808 nm and 980 nm NIR lasers was maintained at 0.3 W. All luminescence patterns were captured using an iPhone 11, and the heating stage was used to read out the information.

## Data availability

The data that support the findings of this study are available from the corresponding author upon reasonable request.

## Conflicts of interest

There are no conflicts to declare.

## Acknowledgements

This work was supported by the National Natural Science Foundation of China (Grant No. 21871122 and 21431002) and the Fundamental Research Funds for the Central Universities (Grant No. lzujbky-2021-kb17).

 

## References


1 S. Cho, S. Kim, J. Kim, *et al.*, Hybridisation of perovskite nanocrystals with organic molecules for highly efficient liquid scintillators, *Light: Sci. Appl.*, 2020, **9**, 159.

2 J. Zhao, L. Zhao, Y. Deng, *et al.*, Perovskite-filled membranes for flexible and large-area direct-conversion X-ray detector arrays, *Nat. Photonics*, 2020, **14**, 612–617.

3 W. Zhu, W. Ma, Y. Su, *et al.*, Low-dose real-time X-ray imaging with nontoxic double perovskite scintillators, *Light: Sci. Appl.*, 2020, **9**, 112.

4 Z. Li, G. Peng, Z. Li, *et al.*, Hydrogen Bonds Strengthened Metal-Free Perovskite for Degradable X-ray Detector with Enhanced Stability, Flexibility and Sensitivity, *Angew. Chem., Int. Ed.*, 2023, **62**, 10.

5 J. Liu, B. Shabbir, C. Wang, *et al.*, Flexible, Printable Soft-X-Ray Detectors Based on All-Inorganic Perovskite Quantum Dots, *Adv. Mater.*, 2019, **31**, 30.

6 W. Pan, B. Yang, G. Niu, *et al.*, Hot-Pressed $CsPbBr_3$ Quasi-Monocrystalline Film for Sensitive Direct X-ray Detection, *Adv. Mater.*, 2019, **31**, 44.

7 F. Zhang, Y. Zhou, Z. Chen, *et al.*, Thermally Activated Delayed Fluorescence Zirconium-Based Perovskites for Large-Area and Ultraflexible X-ray Scintillator Screens, *Adv. Mater.*, 2022, **34**, 43.

8 F. Zhou, Z. Li, W. Lan, *et al.*, Halide Perovskite, a Potential Scintillator for X-Ray Detection, *Small Methods*, 2020, **4**, 10.

9 F. Qiu, G. Peng, Y. Xu, *et al.*, Sequential Vacuum Evaporated Copper Metal Halides for Scalable, Flexible, and Dynamic X-Ray Detection, *Adv. Funct. Mater.*, 2023, **33**, 36.

10 X. Zhou, K. Han, Y. Wang, *et al.*, Energy-Trapping Management in X-Ray Storage Phosphors for Flexible 3D Imaging, *Adv. Mater.*, 2023, **35**, 16.

11 A. Jana, S. Cho, S. A. Patil, *et al.*, Perovskite: Scintillators, direct detectors, and X-ray imagers, *Mater. Today*, 2022, **55**, 110–136.

12 Z. Yang, T. Wang, X. Xu, *et al.*, Fiber Optic Plate Coupled Pb-Free Perovskite X-ray Camera Featuring Low-Dose-Rate Imaging toward Dental Diagnosis, *J. Phys. Chem. Lett.*, 2023, **14**, 326–333.

13 Y. Wu, J. Feng, Z. Yang, *et al.*, Halide Perovskite: A Promising Candidate for Next-Generation X-Ray Detectors, *Adv. Sci.*, 2022, **10**, 1.

14 X. He, M. Xia, H. Wu, *et al.*, Quasi-2D Perovskite Thick Film for X-Ray Detection with Low Detection Limit, *Adv. Funct. Mater.*, 2021, **32**, 7.

15 H. Li, J. Song, W. Pan, *et al.*, Sensitive and Stable 2D Perovskite Single Crystal X-ray Detectors Enabled by a Supramolecular Anchor, *Adv. Mater.*, 2020, **32**, 40.

16 W. Ma, T. Jiang, Z. Yang, *et al.*, Highly Resolved and Robust Dynamic X-Ray Imaging Using Perovskite Glass Ceramic Scintillator with Reduced Light Scattering, *Adv. Sci.*, 2021, **8**, 15.

17 W. Pan, H. Wu, J. Luo, *et al.*, $Cs_2AgBiBr_6$ single-crystal X-ray detectors with a low detection limit, *Nat. Photonics*, 2017, **11**, 726–732.

18 H. Wei, Y. Fang, P. Mulligan, *et al.*, Sensitive X-ray detectors made of methylammonium lead tribromide perovskite single crystals, *Nat. Photonics*, 2016, **10**, 333–339.

19 M. Xia, J. H. Yuan, G. Niu, *et al.*, Unveiling the Structural Descriptor of $A_3B_2X_9$ Perovskite Derivatives toward X-Ray Detectors with Low Detection Limit and High Stability, *Adv. Funct. Mater.*, 2020, **30**, 24.

20 B. Yang, L. Yin, G. Niu, *et al.*, Lead-Free Halide $Rb_2CuBr_3$ as Sensitive X-Ray Scintillator, *Adv. Mater.*, 2019, **31**, 44.

21 H. Zhang, Z. Yang, M. Zhou, *et al.*, Reproducible X-ray Imaging with a Perovskite Nanocrystal Scintillator Embedded in a Transparent Amorphous Network Structure, *Adv. Mater.*, 2021, **33**, 40.

22 S. Ding, H. Guo, P. Feng, *et al.*, A New Near-Infrared Long Persistent Luminescence Material with Its Outstanding Persistent Luminescence Performance and Promising Multifunctional Application Prospects, *Adv. Opt. Mater.*, 2020, **8**, 18.

23 Y. Lin, C. Ming, Z. Wang, *et al.*, Co-doped long persistent luminescence materials $LiSr_3SiO_4Cl_3$:$Eu^{2+}$,$Ln^{3+}$ (Ln = Dy, Ho, Er): construction and verification of VRBE and HRBE scheme and their multifunctional applications, *Inorg. Chem. Front.*, 2023, **10**, 5071–5081.

24 T. Lyu and P. Dorenbos, Towards information storage by designing both electron and hole detrapping processes in bismuth and lanthanide-doped $LiRE(Si,Ge)O_4$ (RE = Y, Lu) with high charge carrier storage capacity, *Chem. Eng. J.*, 2020, **400**, 124776.

25 T. Lyu and P. Dorenbos, Vacuum-Referred Binding Energies of Bismuth and Lanthanide Levels in $LiTaO_3$ Perovskite: Toward Designing Energy Storage Phosphor for Anti-Counterfeiting, X-Ray Imaging, and Mechanoluminescence, *Laser Photonics Rev.*, 2022, **16**, 10.

26 T. Lyu, P. Dorenbos and Z. Wei, Designing $LiTaO_3$:$Ln^{3+}$, $Eu^{3+}$ (Ln = Tb or Pr) perovskite dosimeter with excellent charge carrier storage capacity and stability for anti-counterfeiting and flexible X-ray imaging, *Chem. Eng. J.*, 2023, **461**, 141685.

27 Y. Yang, P. Zhang, W. Xie, *et al.*, Time-dependent multicolor evolution of photoluminescence and afterglow in lanthanide-doped gallate, *Chem. Eng. J.*, 2023, **476**, 146487.

28 B. Yu, Y. J. Wang, Y. Y. Lin, *et al.*, HKUST-1 nano metal–organic frameworks combined with $ZnGa_2O_4$:$Cr^{3+}$ near-infrared persistent luminescence nanoparticles for in vivo imaging and tumor chemodynamic and photothermal synergic therapy, *Nanoscale*, 2022, **14**, 8978–8985.

29 S. Zhao, Z. Wang, Y. Lin, *et al.*, Multi-level information security realized in ortho-stannic acid magnesium with a single activator of $Tb^{3+}$, *Inorg. Chem. Front.*, 2021, **8**, 3522–3531.

30 D. Gao, Q. Kuang, F. Gao, *et al.*, Achieving opto-responsive multimode luminescence in $Zn_{1+X}Ga_{2-2X}GO_4$:Mn persistent phosphors for advanced anti-counterfeiting and information encryption, *Mater. Today Phys.*, 2022, **27**, 100765.

31 C. Jia, J. Yu, Y. Hu, *et al.*, Deep-trap persistent materials for future rewriteable optical information storage, *Phys. Chem. Chem. Phys.*, 2024, **26**, 19591–19605.
32 D. Heggen, R. Zilenaite, E. Ezerskyte, *et al.*, A Standalone, Battery-Free Light Dosimeter for Ultraviolet to Infrared Light, *Adv. Funct. Mater.*, 2021, **32**, 14.
33 P. Zhang, W. Xie, Z. Wang, *et al.*, Time-dependent dynamic multicolor afterglow of simple $LiGa_5O_8$:$Eu^{3+}$/$Tb^{3+}$particles for advanced anticounterfeiting and encryption, *Inorg. Chem. Front.*, 2022, **9**, 4022–4029.
34 Z.-H. Zuo, Y. Y. Peng, J. Li, *et al.*, Thermal-responsive dynamic color-tunable persistent luminescence from green to deep red for advanced anti-counterfeiting, *Chem. Eng. J.*, 2022, **446**, 16976.
35 P. Huang, Z. Wen, Y. Yu, *et al.*, High charge carrier storage capacity and wide range X-rays to infrared photon sensing in $LiLuGeO_4$:$Bi^{3+}$,$Ln^{3+}$ (Ln = Pr, Tb, or Dy) for anti-counterfeiting and information storage applica-tions, *Mater. Chem. Front.*, 2023, **7**, 168–182.
36 G. Liu, Y. Wang and T. Seto, A Giant Stokes Shift in Wide-Band Red Phosphor $[Ca_{0.33}(Sr_{1-x}Ba_x)_{0.67}]_7(SiO_3)_6Cl_2$: $Eu^{2+}$, *Adv. Opt. Mater.*, 2024, **12**, 16.
37 L. Li, T. Li, Y. Hu, *et al.*, Mechanism of the trivalent lanthanides' persistent luminescence in wide bandgap materials, *Light: Sci. Appl.*, 2022, **11**, 5071–5081.
38 P. Dorenbos, $Ce^{3+}$ 5d-centroid shift and vacuum referred 4f-electron binding energies of all lanthanide impurities in 150 different compounds, *J. Lumin.*, 2002, **99**, 283.
39 R. Zhou, L. Lin, C. Liu, *et al.*, Insight into Eu redox and $Pr^{3+}$ 5d emission in $KSrPO_4$ by VRBE scheme construction, *Dalton Trans.*, 2018, **47**, 306–313.
40 Y. Zhuang, Y. Lv, L. Wang, *et al.*, Trap Depth Engineering of $SrSi_2O_2N_2$:$Ln^{2+}$,$Ln^{3+}$ ($Ln^{2+}$ = Yb, Eu; $Ln^{3+}$ = Dy, Ho, Er) Persistent Luminescence Materials for Information Storage Applications, *ACS Appl. Mater. Interfaces*, 2018, **10**, 1854–1864.
41 Z. Q. Jiang, Y. H. Wang and L. S. Wang, Enhanced Yellow-to-Orange Emission of Si-Doped $Mg_3Y_2Ge_3O_{12}$: $Ce^{3+}$ Garnet Phosphors for Warm White Light-Emitting Diodes, *J. Electrochem. Soc.*, 2010, **157**(5), J155–J158.
42 M. Liao, Z. Mu, S. Zhang, *et al.*, A red phosphor $Mg_3Y_2Ge_3O_{12}$: $Bi^{3+}$, $Eu^{3+}$ with high brightness and excellent thermal stability of luminescence for white light-emitting diodes, *J. Lumin.*, 2019, **210**, 202–209.
43 D. Hou, R. Huang, J.-Y. Li, *et al.*, Expanded visible-near-infrared temperature sensing properties in view of ultra-broadband tunable luminescence in $Mg_3Y_2Ge_3O_{12}$:$Ce^{3+}$, $Cr^{3+}$ phosphors with advanced applications, *J. Lumin.*, 2022, **251**, 119204.
44 X. Meng, Z. Wang, S. Wu, *et al.*, Improving the luminescence and afterglow properties of $Mg_3Y_2Ge_3O_{12}$:$Cr^{3+}$ by co-doping $Bi^{3+}$, *Ceram. Int.*, 2020, **46**, 18903–18910.
45 G. Krieke, G. Doke, A. Antuzevics, *et al.*, Tuneable persistent luminescence of novel $Mg_3Y_2Ge_3O_{12}$ garnet, *J. Alloys Compd.*, 2022, **922**, 166312.
46 C. Ji, Z. Huang, X. Tian, *et al.*, Novel red emitting phosphors $Mg_3Y_2Ge_3O_{12}$:$Sm^{3+}$ with high color purity and excellent thermal stability used in W-LEDs, *J. Alloys Compd.*, 2020, **825**, 154176.
47 H. Lin, J. Xu, Q. Huang, *et al.*, Bandgap Tailoring via Si Doping in Inverse-Garnet $Mg_3Y_2Ge_3O_{12}$:$Ce^{3+}$ Persistent Phosphor Potentially Applicable in AC-LED, *ACS Appl. Mater. Interfaces*, 2015, **7**, 21835–21843.
48 A. Mao, Z. Zhao, J. Wang, *et al.*, Crystal structure and photo-luminescence of $Gd_3Ga_2(Al_{3(-x}Si_x)(O_{12(-y}N_y)$:$Ce^{3+}$ phosphors for AC-warm LEDS, *Chem. Eng. J.*, 2019, **368**, 924–932.
49 F. Xie, J. Li, D. Xu, *et al.*, Layer-structure-suppressed concentration quenching of $Dy^{3+}$ luminescence and the realization of a single phase white light-emitting phosphor cooperated with $Tm^{3+}$, *Inorg. Chem. Front.*, 2022, **9**, 3797–3807.
50 P. Dorenbos, Charge transfer bands in optical materials and related defect level location, *Opt. Mater.*, 2017, **69**, 8–22.
51 P. Dorenbos, $Ce^{3+}$ 5d-centroid shift and vacuum referred 4f-electron binding energies of all lanthanide impurities in 150 different compounds, *J. Lumin.*, 2013, **135**, 93–104.
52 P. Dorenbos, Determining binding energies of valence-band electrons in insulators and semiconductors via lanthanide spectroscopy, *Phys. Rev. B:Condens. Matter Mater. Phys.*, 2013, **87**, 3.
53 J. Ueda, R. Maki and S. Tanabe, Vacuum Referred Binding Energy (VRBE)-Guided Design of Orange Persistent $Ca_3Si_2O_7$:$Eu^{2+}$ Phosphors, *Inorg. Chem.*, 2017, **56**, 10353–10360.

 